

# Lawrence Berkeley National Laboratory

## LBL Publications

### Title

Quantification of room temperature strengthening of laser shock peened Ni-based superalloy using synchrotron microdiffraction

### Permalink

<https://escholarship.org/uc/item/16s657b5>

### Authors

Zhou, Guangni  
Zhang, Yubin  
Pantleon, Wolfgang  
[et al.](#)

### Publication Date

2022-09-01

### DOI

10.1016/j.matdes.2022.110948

Peer reviewed

# Quantification of room temperature strengthening mechanisms of laser shock peened Ni-based superalloy using synchrotron microdiffraction

Guangni Zhou<sup>a,b</sup>, Yubin Zhang<sup>b,\*</sup>, Wolfgang Pantleon<sup>b</sup>, Jiawei Kou<sup>a</sup>, Upadrasta Ramamurty<sup>c</sup>, Xipeng Tan<sup>c</sup>, Weifeng He<sup>d</sup>, Ching-Shun Ku<sup>e</sup>, Ching-Yu Chiang<sup>e</sup>, Nobumichi Tamura<sup>f</sup>, Kai Chen<sup>a,\*</sup>

<sup>a</sup> Center for Advancing Materials Performance from the Nanoscale (CAMP-Nano), State Key Laboratory for Mechanical Behavior of Materials, Xi'an Jiaotong University, Xi'an, Shaanxi 710049, P.R. China

<sup>b</sup> Department of Mechanical Engineering, Technical University of Denmark, Kongens Lyngby 2800, Denmark

<sup>c</sup> School of Mechanical and Aerospace Engineering, Nanyang Technological University, Singapore 639798, Singapore

<sup>d</sup> Science and Technology on Plasma Dynamics Laboratory, Air Force Engineering University, Xi'an 710038, P.R. China

<sup>e</sup> National Synchrotron Radiation Research Center, Hsinchu, Taiwan 30076, R.O. China

<sup>f</sup> Advanced Light Source, Lawrence Berkeley National Laboratory, CA 94720, USA

\* Authors for correspondence, email: kchenlbl@gmail.com (K.C.), yubz@mek.dtu.dk (Y.Z.)

## Abstract

Laser shock peening (LSP), a surface treatment technique, exhibits promising applications to improve strength and wear resistance for Ni-based superalloys. To understand the strengthening mechanism in a laser shock peened Ni-based superalloy DZ17G, we utilize advanced synchrotron poly- and monochromatic X-ray microdiffraction, as well as scanning electron microscopy and micro hardness testing to quantify the microstructure and mechanical properties at different depths from the peened surface. It is found that a hardened layer of more than 1.2 mm depth is generated, in which the micro hardness increases continuously and monotonically by

about 50 % from the unaffected interior to the surface. Quantitative analysis of microdiffraction data has shown that large amounts of dislocations are introduced by LSP. High densities of  $7.1 \times 10^{15} \text{ m}^{-2}$  and  $11.8 \times 10^{15} \text{ m}^{-2}$  are seen close to the peened surface for the  $\gamma$  and the  $\gamma'$  phases, respectively, which are about 5 and 20 times of those in the unaffected region. Different gradients of dislocation density are observed for the two phases from the sample interior to the peened surface, and their combined effect accounts well for the hardness gradient. This large population of dislocations dominates the observed strengthening. Combined poly- and monochromatic X-ray microdiffraction allows quantifying the local microstructures of plastic deformation over a large sampling scale that can hardly be achieved using other materials characterization techniques.

Keywords: Hardening; Dislocation density; Laser treatment; Ni-based superalloys; Synchrotron diffraction

## 1. Introduction

Ni-based superalloys, due to their exceptional combination of high-temperature strength, toughness, and resistance to corrosion and oxidation, are widely used to manufacture gas turbine blades and bladed disks (blisks) for aircraft engines and power generating systems, which are exposed to extreme environments in service [1,2]. The superior properties of these superalloys are mainly due to the strengthening effects provided by cuboidal precipitates of ordered  $\gamma'$ -phase in the  $\gamma$ -phase matrix [3]. On the other hand, fretting fatigue damage occurring in the connecting structures between blades and disk such as dovetail attachments is one of the major failure sources in gas turbine engines [4,5]. Surface mechanical treatments such as shot peening and laser shock peening (LSP) are thus necessary to strengthen the dovetail attachments of turbine blades [6,7]. During LSP, a high-power laser pulse ablates a protective overlay (tape, paint or aluminium foil) into plasma. A transparent confining

overlay (glass or water) prevents the generated plasma from expanding and moving away from the treated sample surface. Shock waves with peak pressures of the order of several GPa are produced. As they propagate into the interior of the samples, the peened material is severely plastically deformed at an ultrahigh strain rate ( $10^6 \text{ s}^{-1}$  or higher), resulting in substantial hardening [8]. A particular advantage of LSP over shot peening is its ability to induce a hardened layer (termed case) substantially deeper into the material below the peened surfaces. Case depths of more than 1 mm can be achieved using LSP, causing at the same time much smaller surface roughness than shot peening [9]. These two factors improve fatigue strength, friction and fretting wear resistances greatly [10–15].

For Ni-based superalloys, LSP has been shown to increase room-temperature tensile strength and vibrational fatigue strength by 25-33% and 169%, respectively [14,15], and introduce compressive residual stresses up to 600 MPa near the surface [16]. Moreover, even after annealing for 10 hours at 900 °C, which is a higher temperature than the typical service temperature of dovetail joints of turbine engines, the beneficial effects brought up by LSP are still effective without significant relief [17]. All these advantages make LSP a promising technique for extending the lifetime of Ni-based superalloy blades.

While LSP is already deployed in certain industrial fields of Ni-based superalloy and other alloys, some crucial problems the strengthening mechanisms involved still require in-depth understanding. Transmission electron microscopy (TEM) investigation of the microstructures have revealed that the severe plastic deformation during LSP produces high densities of dislocations, and sometimes, microstructure refinement [18–23]. A detailed quantitative analysis that assesses the potential contributions from dislocations and microstructure refinement to the overall enhancement in strength is yet to be performed. LSP produces a deformed layer in the millimeter range with decreasing plastic strain from the surface to the interior. The correlation between the local microstructure and the local strength has not been established yet, because the high dislocation density produced by LSP is scarcely

possible to measure using TEM, in which the sampling scale of micron is three orders of magnitude smaller than the thickness of the cases, hence a plentitude of specimens would be required to cover the entire case (as obvious from [22]). More importantly, it has not been attempted to establish a direct evidence for microstructural differences between  $\gamma$  and  $\gamma'$  phases after severe plastic deformation at the ultrahigh strain rate induced by LSP, as e.g. the local dislocation density. It is important to quantify the contributions of the different strengthening mechanisms from each phase locally in the laser shock peened Ni-based superalloys. All these issues demand a novel investigation method allowing quantitative measurement of both, the local mechanical strength and the local dislocation density in  $\gamma$  and  $\gamma'$  phases while covering the whole depth of the peened case.

In this paper, we utilize the advanced scanning synchrotron technique micro X-ray diffraction ( $\mu$ XRD) [24] to study the gradient microstructure in a directionally solidified Ni-based superalloy after LSP. With a micro-focused, high-brilliant X-ray beam and a high-precision scanning stage, the local microstructure is readily mapped to cover a millimetre-sized area from the peened surface to the interior with spatial resolution on the scale of micrometers. By combining polychromatic and monochromatic X-ray diffraction signals [25], the local dislocation content in each individual phase,  $\gamma$  and  $\gamma'$ , is quantified. The quantitative analysis of the dislocation contents in each phase provides key insights for understanding the effects of LSP and for revealing the strengthening mechanisms of laser shock peened Ni-based superalloys.

## **2. Materials and Experiments**

### **2.1. Materials and LSP treatment**

A directionally solidified Ni-based superalloy DZ17G is investigated. The nominal composition of the alloy is listed in Table 1. The material shows dendritic growth. As illustrated schematically in Figure 1a, the primary dendrites were about

200  $\mu\text{m}$  in width and grew along an  $\langle 001 \rangle$  crystal direction. Grain boundaries, defined by boundaries with misorientation angles of  $15^\circ$  and above, were almost all parallel to the primary dendrite growth direction (indicated as Y-direction). Transverse grains boundaries were essentially absent, and the resulting grain width ranged from 200  $\mu\text{m}$  to 2 mm. The DZ17G superalloy was composed mainly of  $\text{Ni}_3(\text{Al}, \text{Ti}) \gamma'$ -precipitates with ordered  $\text{L1}_2$  structure within the solid-solution-strengthened  $\gamma$ -matrix with face-centered cubic structure. The volume fraction of the cuboidal  $\gamma'$ -particles was about 70%, and they precipitated coherently within the  $\gamma$  matrix obeying the cube-on-cube orientation relationship,  $(001)_{\gamma'} // (001)_{\gamma}$  and  $\langle 100 \rangle_{\gamma'} // \langle 100 \rangle_{\gamma}$  [26]. The cuboids were distributed regularly in the  $\gamma$  matrix, which appeared as interconnected 3D channels separating the cuboids. MC and  $\text{M}_{23}\text{C}_6$  carbides were detected in the superalloy with a volume fraction less than 1%; thus their impact on the mechanical properties is not considered in this study.

**Table 1.** Nominal composition of DZ17G Ni-based superalloy (wt. %)

Composition	Co	Cr	Al	Ti	Mo	V	Fe	C	B	Ni
Content	9.0-11.0	8.5-9.5	4.8-5.7	4.1-4.7	2.5-3.5	0.6-0.9	$\leq 0.5$	0.13-0.22	0.012-0.024	Balance

Besides newly manufactured blades, LSP is also used for repair of blades after some time in service. Thus, the specimen investigated in this study was vibration fatigued with a peak stress of about 257 MPa for  $10^7$  cycles to simulate service conditions, following the standard of the Ministry of Aviation Industry of the P.R.C. (HB5277-84) prior to LSP. The surface to be treated was mirror polished using SiC papers of grits varying from #180 to #2400. A 0.125 mm thick aluminum foil was used as protective and absorbing layer, and water was applied as confining overlay to promote the generation of shock waves. The specimen was laser shock peened using a Q-switched Nd:YAG laser system. The shock peening direction (indicated as X-direction in Figure 1a) was perpendicular to the dendritic growth direction. LSP was performed with the processing parameters listed in Table 2, an overlapping rate of

50% and repeated three times.

**Table 2.** Processing parameters of the LSP

Laser energy	Spot diameter	Pulse width	Frequency	Power density
5.6 J	2.2 mm	20 ns	1 Hz	7.4 GW/cm <sup>2</sup>

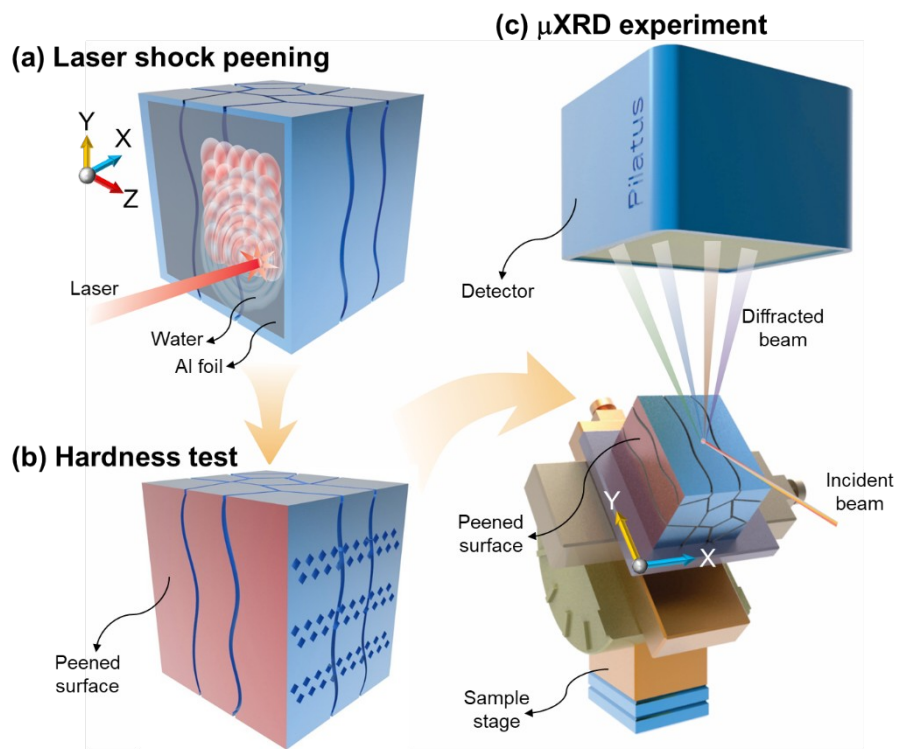


**Figure 1.** Schematic diagrams showing the set-up for LSP, hardness testing and  $\mu$ XRD, with the aid of a Cartesian coordinate system O-XYZ. (a) LSP is carried out on the YZ-surface with the peening direction perpendicular to the primary dendrite growth direction. Grain boundaries, parallel to the primary dendrites, are indicated using the dark blue curves. After LSP, (b) hardness and (c)  $\mu$ XRD are conducted on a cross-sectional XY-plane.

## 2.2. Hardness test

Three regions were arbitrarily chosen on the cross sectional XY-plane to investigate the depth dependence of the hardness at different locations in the case (illustrated in Figure 1b). In each region, the Vickers hardness was tested along two

lines approximately 100  $\mu\text{m}$  separated from each other, both parallel to the peening direction using a HXD-1000TMC/LCD instrument, with a load of 200 gf and a dwell time of 30 s. A total of 14 - 15 indentations were performed along each line. The distance between two adjacent indents was fixed at 120  $\mu\text{m}$  (Figure 1b). On one line, the first indent was placed at a depth of 60  $\mu\text{m}$  from the surface, while at 120  $\mu\text{m}$  from the surface on the other. The diagonal length of the indents was about 30  $\mu\text{m}$ , i.e. less than one-fourth of the space between adjacent indents, which is considered sufficient to eliminate disturbing effects of the deformation zones between neighbouring indents [27].

### 2.3. Synchrotron $\mu\text{XRD}$

Synchrotron polychromatic  $\mu\text{XRD}$  (*a.k.a.* Laue  $\mu\text{XRD}$ ) was conducted at beamline 12.3.2 of the Advanced Light Source at Lawrence Berkeley National Laboratory [28]. A polychromatic X-ray beam (5 - 24 keV) was focused to about  $1 \times 1 \mu\text{m}^2$  using a pair of Kirkpatrick-Baez mirrors. The samples were mounted on a high-resolution XY scan stage that was  $45^\circ$  inclined with respect to the incident X-ray beam. An area of  $1705 \times 234 \mu\text{m}^2$  on the XY-plane, was scanned with the polychromatic X-ray beam with a step size of 5  $\mu\text{m}$  along the peening direction (X-direction) and 3  $\mu\text{m}$  along the dendrite growth direction (Y-direction). At each scan position, a Laue diffraction pattern was recorded using a two-dimensional Pilatus-1M detector (DECTRIS, Baden-Dättwil, Switzerland), mounted in  $90^\circ$  reflection geometry about 150 mm above the sample (Figure 1c). All 26598 recorded Laue diffraction patterns were analysed using the software package XMAS [29], adopting the custom-developed peak position comparison method [30].

To analyse the peak shape in Laue  $\mu\text{XRD}$ , the 004 diffraction peak was converted from detector coordinates to reciprocal space coordinates  $2\theta$ - $\chi$  (Figures 2a and b).  $2\theta$  is the diffraction angle between incident and diffracted beam, while  $\chi$  is the angle between the diffraction plane defined by the incident and the diffracted beam and the plane defined by the incident beam and the detector normal. The intensity

distributions in the  $2\theta$ - $\chi$  space usually appear anisotropic with an elliptical shape. Therefore, for the intensity distribution of each peak in reciprocal space coordinates  $2\theta$ - $\chi$ , the long and short axes were determined. The full widths at half maximum (FWHMs) of the intensity profiles along these long and short axes are denoted as  $\beta_L$  and  $\beta_S$ , respectively (Figures 2c and d). In the present Laue diffraction experiment, the  $00N$  reflection signals ( $N = 2, 4, 6, 8$ ) from  $\gamma$  phase and the  $00M$  reflections ( $M = 2, 3, \dots, 8, 9$ ) from  $\gamma'$  phase appeared at the same position. Therefore, referring to a certain peak such as 004 (to comply with following monochromatic investigations), actually means the superposition of several contributing harmonic reflections.

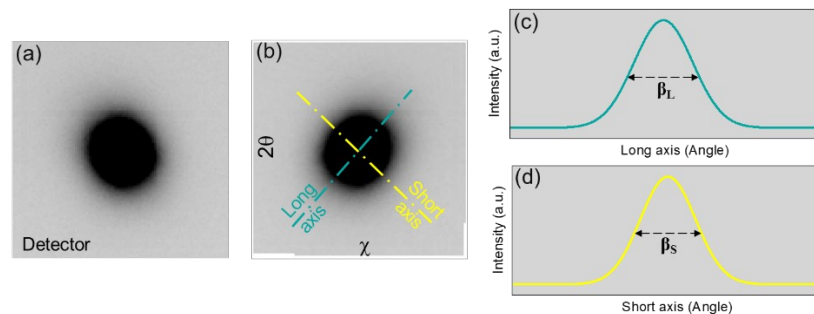


**Figure 2.** Example illustrating how the shape of the Laue diffraction peak is quantified. A 004 Laue diffraction peak is (a) presented in detector coordinates and (b) converted into  $2\theta$ - $\chi$  coordinates. The corresponding intensity profiles along the long and the short axes are displayed in (c) and (d), respectively.

In order to determine locally the radial line profile of the diffraction peaks for quantification of the dislocation density [31,32], mapping was performed using a monochromatic beam by scanning the X-ray energy in minute energy steps, which is termed energy scans in this article. For the present study, the 004 peak was chosen for energy scan in the range of 9950 - 10250 eV with a step size of 1 eV on Beamline 21A at the Taiwan Photon Source. The measurements were conducted in a depth range of 0 to 1.7 mm along two lines that were 100  $\mu\text{m}$  apart from each other and parallel to the peening direction on the XY-plane. Based on the energy scan, the raw radial intensity profile (black circles in Figure 3) was determined in dependence on the

diffraction vector  $Q = 4\pi \frac{\sin \theta}{\lambda}$ , where  $\lambda$  is the wavelength and  $\theta$  half of the angle

between the incident and diffracted beams. After fitting the experimental data, the radial line profile was decomposed into two subprofiles, representing the diffraction signals from  $\gamma$  and  $\gamma'$  phases, respectively (orange and green curves in Figure 3). For decomposition, it was assumed that the integrated intensity ratio of the two subprofiles was equal to the ratio between the volume fractions of the corresponding phases, i.e. 30:70 between  $\gamma$  and  $\gamma'$  phase. The FWHMs for both phases,  $\delta_\gamma$  and  $\delta_{\gamma'}$ , were then determined for quantification of the dislocation density using a procedure [33] adapted from the classical Wilkens' theory [34]. Further details about peak fitting and dislocation density calculations are found in Ref. [33].

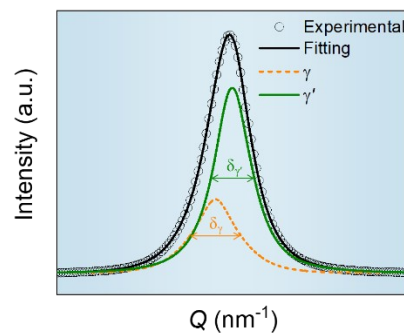


**Figure 3.** Radial line profile of a 004 peak of the Ni-based superalloy determined from an energy scan with monochromatic X-ray beam. The black circles represent experimental diffraction data at one particular position, while the black curve is a fit to the circles using multiple Gaussian function. The orange and green subprofiles originating from  $\gamma$  and  $\gamma'$  phases, respectively, are obtained by decomposition of the black profile following the procedure described in [33].

## 2.4. Electron microscopy

To observe the morphology of the  $\gamma'$  precipitates and their spatial distribution in the  $\gamma$  matrix, XY-plane sections of the specimens were electrochemically etched in  $H_3PO_4$  aqueous solution (25%:75%) under a constant voltage of 5 V. A Hitachi SU6600 field emission scanning electron microscope (SEM) was used for imaging the cuboidal  $\gamma'$  precipitates at various depths along the peening direction on the cross

section. The sizes of individual  $\gamma'$  cuboids were determined as geometric mean of the lengths of two of its adjacent sides.

### 3. Results

#### 3.1. Hardness profile

The microhardness profile from surface to interior along the peening direction is shown in Figure 4. The hardness of the Ni-based superalloy without LSP is measured to be  $(391 \pm 11)$  HV0.2, which is indicated by the dashed blue line. LSP induces a significant increase in hardness reaching 50% near the peened surface, which has a hardness of 587 HV0.2; the case, defined as the region in which an increased hardness is detected, ranges from the surface to a depth of 1.2 - 1.4 mm.

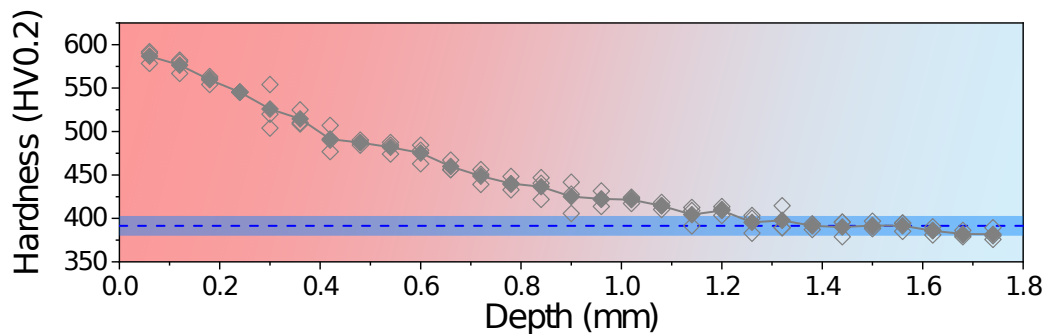


**Figure 4.** Vickers microhardness as a function of peening depth of the laser shock peened Ni-based superalloy. The hollow and solid diamonds are the determined and their average values, respectively. The dashed blue line represents the average hardness of the fatigued superalloy without any LSP.

#### 3.2. Laue $\mu$ XRD

The patterns obtained by Laue  $\mu$ XRD are evaluated in two manners. The peak positions allow determination of the local crystallographic orientations, and the shape of the peaks acts as an initial manifestation of the presence of dislocation structure. The crystallographic orientations in the area scanned by polychromatic X-rays are displayed in Figure 5a, where the colours represent the crystallographic directions along the Z-direction, i.e. the normal of the cross section. Two large grains are

identified in the examined area by their appearance in different colours in the map (Grain 1 in red and Grain 2 in orange). The alternating appearance of both colours in the region on the right is due to the co-existence of both grains in the volume penetrated by the synchrotron X-ray beam and giving rise to diffraction. Only the orientation from the grain dominating the diffraction signal, i.e. with larger volume fraction along the path of the incoming X-rays, is presented in Figure 5a. The exact location of the grain boundary between these two grains in 3D is unknown, which is however less important for the present analysis. No other orientation is detected in the mapped region. Apparently, the original grain structures are preserved and no grain refinement occurred.

Three typical Laue diffraction patterns taken at various depths from the peened surface at positions marked by B, C and D in Figure 5a are shown in Figures 5b, c, and d, respectively. The diffraction peaks obtained from the location close to the peened surface (position B) are significantly broadened compared to those obtained from the same grain but about 1 mm away from the surface (position C). The diffraction peaks from the second grain (position D) are comparatively sharp and intense. The misorientation profiles along the lines marked E1-E2 and F1-F2 on Figure 5a are displayed in Figure 5e. The majority of the misorientation angles between neighbouring pixels is below  $1.5^\circ$ . The point-to-origin misorientation angle increases to about  $2^\circ$  from the peened surface to a depth of about  $150\ \mu\text{m}$ , indicating an accumulation of misorientation over this distance. In larger distances from the surface, i.e. in deeper regions, the point-to-origin misorientation angle remains this high level. The observed scatter is caused by occurring point-to-point misorientations.

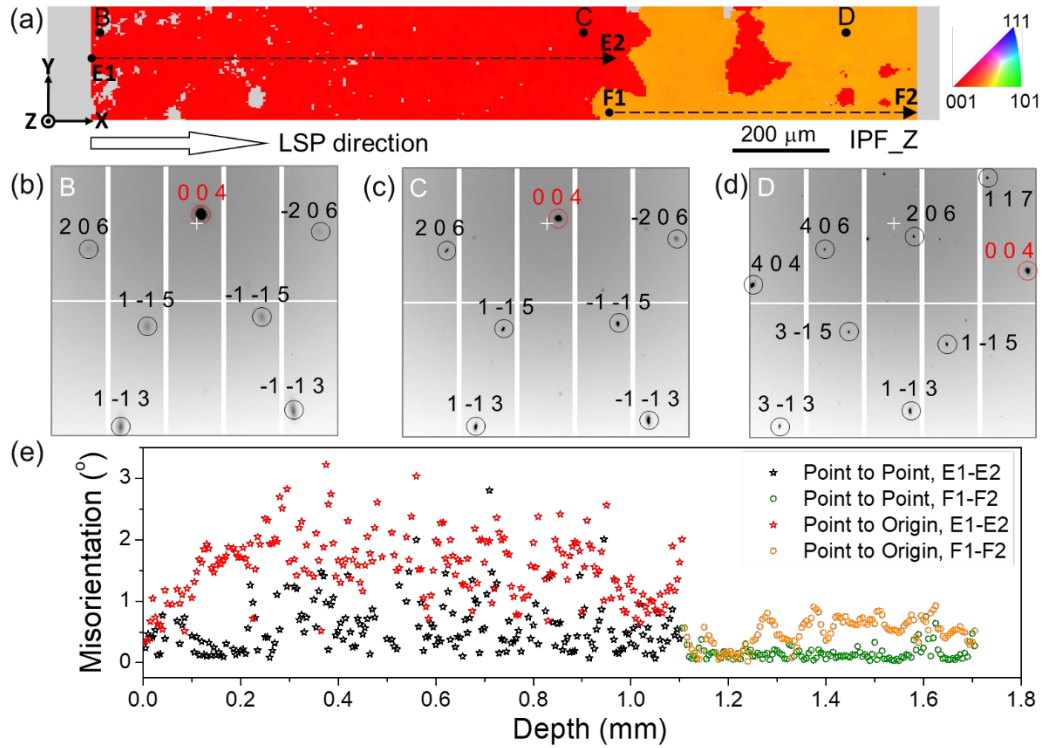


**Figure 5.** Laue  $\mu$ XRD on the cross section of the laser shock peened Ni-based superalloy. (a) Orientation map, colored according to the crystallographic orientation along the Z-direction. The peened sample surface is to the left, non-indexed pixels are shown in grey. (b)-(d) Three representative indexed Laue diffraction patterns collected at positions B, C and D marked in (a), respectively. The white cross in each Laue pattern marks the position where the beam is diffracted by a diffraction angle  $2\theta$  of  $90^\circ$  and  $\chi$  of  $0^\circ$ . (e) Misorientation profiles along the peening direction in the two grains, marked E1-E2 and F1-F2. Both, point-to-origin (with respect to E1/F1) and point-to-point misorientations, are shown.

The 004 reflection is selected for further peak shape analysis for two reasons. Firstly, it is the strongest peak and has a high signal-to-noise ratio. Secondly, the 004 peak is observed for both of the detected orientations (marked by red circles in Figure 5b, c and d). The peak widths along the short ( $\beta_S$ ) and long ( $\beta_L$ ) axes determined at each position in the scanned area are plotted in Figures 6a and b, respectively. Both widths decrease with increasing distance from the peened surface. The ratio between  $\beta_S$  and  $\beta_L$  at each position in the scan is computed and displayed in Figure 6c. Up to a depth of about 1.1 mm, i.e. in Grain 1, this ratio is close to 1, implying that the

diffraction peaks are broadened almost isotropic. The ratio in Grain 2 is generally lower (about 0.5), reflecting that the intensity distributions of the 004 diffraction peaks in the  $2\theta$ - $\chi$  coordinates are slightly elliptical. The  $\beta_s/\beta_L$  ratio varies significantly within each grain. Moreover, the peak widths and  $\beta_s/\beta_L$  ratios are affected by the presence of interdendritic carbides, as pointed out by the black arrows, due to different plastic deformation close to the carbides [35].

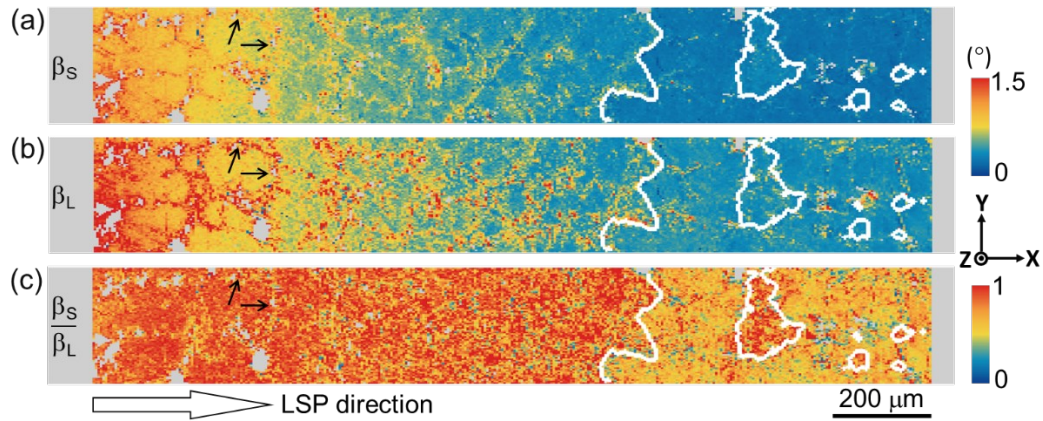


**Figure 6.** Quantitative results of the 004 Laue diffraction peak in the laser shock peened Ni-based superalloy. Maps of peak widths (a) along short and (b) long axes and (c) their ratios of the 004 Laue peak in the laser shock peened Ni-based superalloy. The white curves correspond to colour changes between red and orange in the orientation map, i.e. the high angle grain boundaries.

### 3.3. Energy scans with monochromatic beam for dislocation characterization

From energy scans with monochromatic X-rays, the radial line profile of diffraction peak 004 is obtained and separated into subprofiles for each phase, based on which FWHM and dislocation density are determined. The FWHMs of these radial subprofiles,  $\delta$ , as a function of distance from the peening surface are shown in Figure 7a. At positions deeper than 200 - 300  $\mu\text{m}$  below the peened surface, the FWHM obtained for the  $\gamma$  phase is larger than that for the  $\gamma'$  phase. Near the peened surface, the FWHM is similar for both phases.

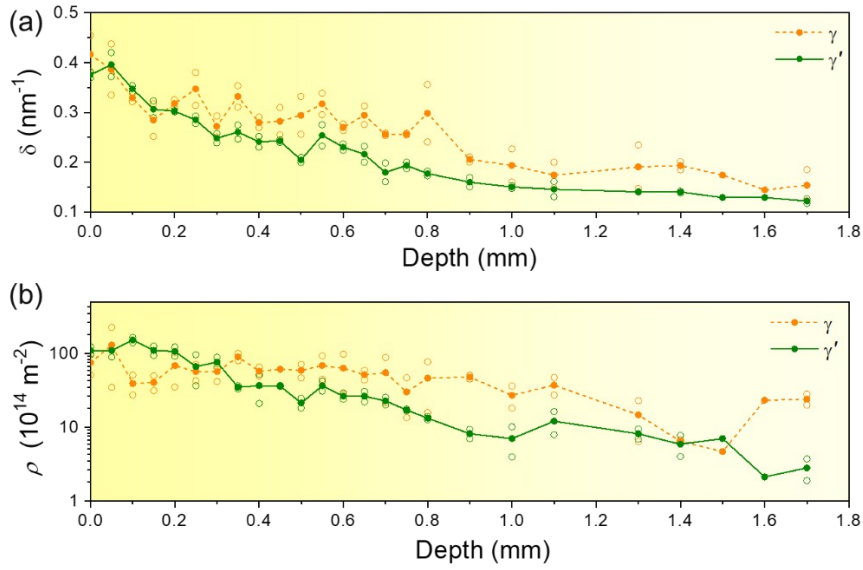


**Figure 7.** Quantitative results based on monochromatic energy scans. (a) FWHM  $\delta$  and (b) redundant dislocation density  $\rho$  obtained from energy scans for both  $\gamma$  and  $\gamma'$  phases as a function of depth in the peened case. Hollow circles represent the original data from two individual measuring lines, while solid dots indicate average values.

Following a recently developed procedure [33], the redundant dislocation densities  $\rho$  were determined locally in each of the two phases based on the radial subprofile in dependence of the depth below the peened surface (Figure 7b). Similar to the depth depending variations in FWHM for both phases, higher dislocation densities are detected in  $\gamma$  phase than in  $\gamma'$  phase in most regions except close to the surface. In the regions unaffected from LSP (deeper than 1.4 mm from the peened surface), the average dislocation density in the  $\gamma$  phase is  $14.6 \times 10^{14} \text{ m}^{-2}$ , while only  $5.3 \times 10^{14} \text{ m}^{-2}$  in the  $\gamma'$  phase. These dislocations are probably introduced during the vibration fatigue test [33]. The dislocation density in the  $\gamma'$  phase increases continuously from the unaffected interior to a depth of 100  $\mu\text{m}$ . Within the region up to 100  $\mu\text{m}$  from the peened surface, the dislocation density is constant, or even drops slightly. For the  $\gamma$  phase, the dislocation densities increase from low values at 1.3 mm from the surface and deeper to an almost constant value in a depth range between 100  $\mu\text{m}$  and 800  $\mu\text{m}$ . The two courses of the dislocation densities cross each other at the depth around 300  $\mu\text{m}$  (Figure 7b), leading to a lower dislocation density in the  $\gamma$  phase than in the  $\gamma'$

phase in a region between 100  $\mu\text{m}$  and 300  $\mu\text{m}$  below the peened surface. In the region up to 200  $\mu\text{m}$  below the peened surface, the average dislocation density detected in  $\gamma$  and  $\gamma'$  phases are  $7.1 \times 10^{15} \text{ m}^{-2}$  and  $11.8 \times 10^{15} \text{ m}^{-2}$ , respectively. These are about 5 and 20 times higher than the respective values in the unaffected region.

### 3.4. Microscopic observations

The shape and size of  $\gamma'$  precipitates after LSP were investigated in a cross section using SEM. The overall shape of  $\gamma'$  precipitates remained cuboidal, despite occasionally observed coalescence (Figure 8a and b). As seen from Figure 8c, the size of the  $\gamma'$  cuboids varies around an average of 360 nm and does not show any noticeable systematic variation within the investigated region, i.e. the case formed by LSP.

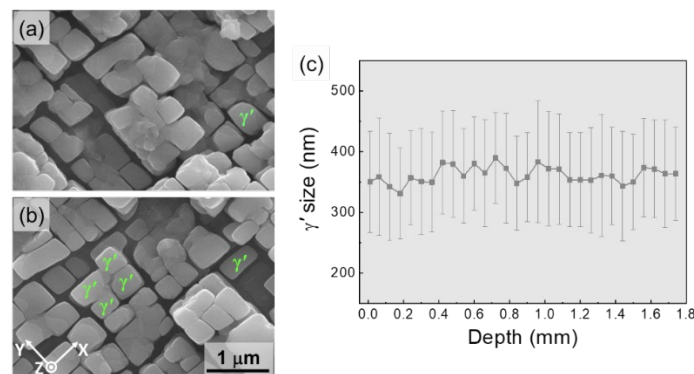


**Figure 8.** SEM investigation of  $\gamma'$  precipitates. The secondary electron images are taken at a depth of (a) about 10  $\mu\text{m}$  and (b) 1.0 mm. (c) shows the size of the  $\gamma'$  cuboids in dependence on depth. At each depth, 96 cuboidal  $\gamma'$  particles are measured and the error bars represent the standard deviation of their size distributions.

## 4. Discussion

The present study has demonstrated that synchrotron  $\mu\text{XRD}$  is a powerful tool for quantitative analysis of the local microstructures. The small beam size of  $1 \times 1 \mu\text{m}^2$  micrometer ensures a high spatial resolution. Based on the Laue diffraction patterns collected with a polychromatic beam, both the crystallographic orientation and the

shape of the peaks can be determined. When using monochromatic beams, dislocation density, lattice parameter and residual elastic strains can be quantified separately for different phases, even for cases like the present Ni-based superalloy where the two phases have similar lattice parameters. It is evident that  $\mu$ XRD can be used for studying severely deformed samples containing dislocation densities in the order above  $10^{15} \text{ m}^{-2}$ , which is challenging to quantify by TEM.

With a suitable subprofile separation and fitting algorithm, the dislocation densities in both  $\gamma$  and  $\gamma'$  phases are quantified in the present DZ17G superalloy locally within the whole laser shock peened case. Such information is crucial for understanding the plastic deformation induced by LSP and for quantifying the contribution of each phase to the strength increase.

#### **4.1. LSP induced plastic deformation**

The hardness and synchrotron  $\mu$ XRD data reveal that in the region up to 1.2 - 1.4 mm from the peened surface a case is formed by LSP where both, the hardness and the dislocation density, are higher than those in the interior. The size and morphology of  $\gamma'$  precipitates are the same throughout the case, proving that no pronounced phase transformation between  $\gamma$  and  $\gamma'$  phases occurs during LSP. Also, no grain refinement is observed, which is similar to what has been reported in LSP treated mono- and polycrystalline Ni-based superalloys [9,36,37] as well as other materials systems [38,39]. The LSP induced hardening is therefore mainly caused by dislocations.

The nearly isotropic broadening of the Laue diffraction peaks in the  $2\theta$ - $\chi$  space (see Figure 6) suggests that the dislocations generated by LSP are mainly redundant, and a small fraction of non-redundant [40]. The non-redundant dislocation content to produce a misorientation  $\theta$  across a distance  $d$  as in the orientation gradient near the surface is given by the Read Shockley equation  $\rho = \theta / bd$  and determined by the Burgers vector  $b$  of the dislocations [41]. Figure 5e shows an orientation gradient accumulating a misorientation angle of  $2^\circ$  across a distance of  $150 \mu\text{m}$  below the

peened surface, resulting in a non-redundant dislocation density of  $9.2 \times 10^{11} \text{ m}^{-2}$ . In larger depth, the misorientation angle of  $2^\circ$  with respect to the orientation at the surface does not vary systematically. Similar orientation gradients within a similar range of depth have also been observed in LSP treated Ti6Al4V [42] and Inconel 718SPF [43]. Even the non-redundant density  $2.1 \times 10^{13} \text{ m}^{-2}$  expected locally from the point-to-point misorientation angle of  $1.5^\circ$  between points in a distance of  $5 \mu\text{m}$  is 2 orders of magnitude lower than the redundant dislocation density (Figure 7b). Consequently, the non-redundant dislocation density is negligible and the total dislocation density is determined dominantly by redundant dislocations. The considerable amount of redundant dislocations generated by LSP affects the mechanical properties to much larger depth than non-redundant dislocation density responsible for the orientation gradient close to the surface.

The dislocations distribute heterogeneously between the  $\gamma$  and  $\gamma'$  phases. For depth deeper than 0.7 mm from the surface, the dislocation density in the  $\gamma$  channels is roughly twice of that in the  $\gamma'$  cuboids. In the region close to the peened surface, the dislocation density in the  $\gamma$  channels remains at a constant value probably due to dynamic annihilation, while the dislocation density is higher in the  $\gamma'$  cuboids. The annihilation of dislocations in the  $\gamma$  channels becomes easier as the dislocations are confined, while the  $L1_2$  structure of the  $\gamma'$  cuboids makes annihilation more difficult as the motion of superdislocations is restricted to their slip plane by an anti-phase boundary.

The dislocation density revealed in DZ17G is much higher than the ones reported for Ni and other Ni-based superalloys after shock loading. For example, after shock loading with a pressure of 25 GPa a dislocation density of  $1.3 \times 10^{15} \text{ m}^{-2}$  is found in single phase Inconel 600 [44]. This dislocation density is only about 1/5 of that in the  $\gamma$  channels of the present sample. Both the presence of dislocations prior to LSP and the pinning by  $\gamma'$  cuboids may be important factors for this difference.

## 4.2. Strengthening mechanism

In general, the strength of metallic materials is a combined effect of lattice friction, solute atoms, dislocations, grain boundaries and precipitates [45]. Since no new grain boundaries are generated by LSP in our study and the precipitate size throughout the case are the same as those in the interior, the effects of grain boundaries and precipitates are ruled out for explaining the observed hardness increase. Likewise, hardness differences in the case caused by different solid solution strengthening can be excluded as no hint of any partial or full dissolution of the  $\gamma'$  precipitates is demonstrated and long range migration and redistribution of solute elements are not likely to occur in the short period of time of LSP. Consequently, the observed hardness profile must root in the locally different dislocation density generated by LSP.

The contribution to the flow stress due to interactions among dislocations is described by the Taylor relation [46]:

$$\Delta\sigma_{disl} = \alpha M G b \sqrt{\rho} \quad (4)$$

where  $\alpha$  is an interaction coefficient,  $M$  the Taylor factor,  $G$  the shear modulus,  $b$  the Burgers vector, and  $\rho$  the total dislocation density. The contributions from the  $\gamma$  and  $\gamma'$  phases are considered separately obeying the rule of mixtures:

$$\Delta\sigma_{disl} = f_{\gamma} \Delta\sigma_{disl,\gamma} + (1 - f_{\gamma}) \Delta\sigma_{disl,\gamma'} \quad (5)$$

where  $f_{\gamma}$  is the volume fraction of the  $\gamma$  phase (30%). Using the determined redundant dislocation densities presented in Figure 7b and the parameters  $\alpha = 0.24$ ,  $M = 2.449$ ,  $b = 0.253$  nm,  $G = 76$  GPa for the  $\gamma$  phase and 78 GPa for the  $\gamma'$  phase in Equation 5 [47], the strength increase (compared to the unaffected interior) contributed by the dislocations in the peened case are calculated. They are compared with the hardness increase  $\Delta HV$  with respect to the average value for an unpeened, fatigued specimen reported in Figure 4 converted to a contribution to the tensile strength  $\Delta\sigma_{HV}$  by Tabors relation  $\sigma_{HV} = HV/3$  [48].

As seen from Figure 9, the calculated strengthening effect  $\Delta\sigma_{dist}$  from the determined dislocation densities agrees well with the observed strength increase  $\Delta\sigma_{HV}$  determined from the hardness, proving that work-hardening by dislocations is responsible for the hardness increase in the case of the laser shock peened Ni-based superalloy DZ17G in this study. A deviation is seen for the first 300  $\mu\text{m}$  below the peened surface, which is probably attributed to the heterogenous dislocation density in the phases and may indicate that there is an overestimation of the resolved dislocation densities due to the difficulties with profile separation in this case.

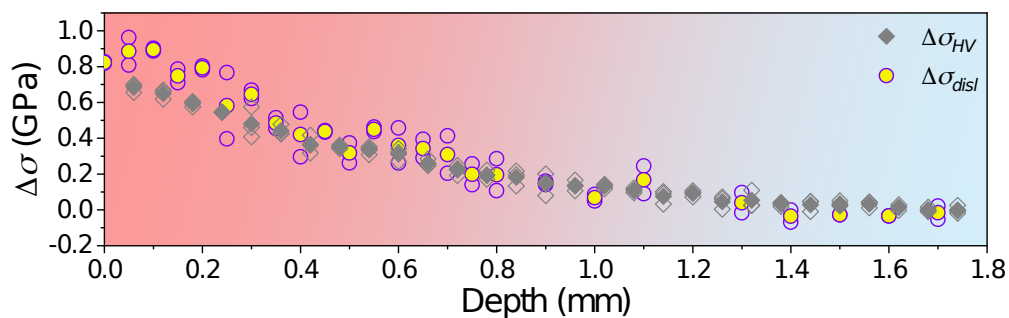


**Figure 9.** Strength contribution of redundant dislocations induced by LSP in comparison with hardness increase depending on the depth from the peened surface. Hollow symbols display values obtained locally at different lines, while solid ones represent their average values.

## 5. Conclusions

In the present study, a laser shock peened Ni-based superalloy DZ17G was characterized using advanced synchrotron  $\mu\text{XRD}$  with the aim to analyse and quantify the relevant strengthening mechanism. The main conclusions are:

(1) LSP develops a hardened case in the Ni-based superalloy to a depth of 1.2 - 1.4 mm from the peened surface. After three impacts, a maximum hardness of 587 HV0.2 is obtained close to the surface, which is about 50% higher than that in the unaffected region.

(2) Plastic deformation caused by LSP results in a high redundant dislocation density. Only a small density ( $2.1 \times 10^{13} \text{ m}^{-2}$ ) of non-redundant dislocations are required as determined from the local misorientations.

(3) The redundant dislocation densities induced by LSP near the surface regions reach  $7.1 - 11.8 \times 10^{15} \text{ m}^{-2}$  in  $\gamma$  and  $\gamma'$  phases, which is about 5 and 20 times higher than that in the unaffected region. The redundant dislocation density in the  $\gamma$  phase remains a plateau value between 100  $\mu\text{m}$  and 800  $\mu\text{m}$  depth from the surface, while the dislocation density in the  $\gamma'$  cuboids increase continuously from the unaffected region towards the surface except the first 100  $\mu\text{m}$  from the surface.

(4) The work-hardening effect of the redundant dislocation density induced by LSP is quantified based on the  $\mu\text{XRD}$  measured dislocation densities. The excellent agreement with the local hardness measurements confirms accumulation of dislocations as the major strengthening mechanism.

## **Acknowledgements**

This work was supported by the National Natural Science Foundation of China (Nos. 91860109 and 51927801) and the National Key Research and Development Program of China (No. 2016YFB0700404). G.Z. would like to acknowledge the financial support from the program of China Scholarships Council (No. 201806280355). K.C. appreciates the support from the International Joint Laboratory for Micro/Nano Manufacturing and Measurement Technologies and the Collaborative Innovation Center of High-End Manufacturing Equipment. Y. Z. acknowledges support from the European Research Council (ERC grant agreement No.788567 M4D).

## **References**

- [1] R. Schafrik, R. Sprague, Gas turbine materials, *Adv. Mater. Process.* 5 (2004) 29–34.
- [2] T.M. Pollock, Alloy design for aircraft engines, *Nat. Mater.* 15 (2016) 809–815.
- [3] T.M. Pollock, S. Tin, Nickel-based superalloys for advanced turbine engines:

- chemistry, microstructure and properties, *J. Propuls. Power.* 22 (2006) 361–374.
- [4] M. Ciavarella, G. Demelio, A review of analytical aspects of fretting fatigue, with extension to damage parameters, and application to dovetail joints, *Int. J. Solids Struct.* 38 (2001) 1791–1811.
- [5] D. Thomson, The national high cycle fatigue (HCF) program, Third National Turbine Engine High Cycle Fatigue Conference, 1998.
- [6] S. Bagheri, M. Guagliano, Review of shot peening processes to obtain nanocrystalline surfaces in metal alloys, *Surf. Eng.* 25 (2009) 3–14.
- [7] A.H. Clauer, Laser shock peening for fatigue resistance, *Surf. Perform. Titan.* 217 (1996) 230.
- [8] C.S. Montross, T. Wei, L. Ye, G. Clark, Y.W. Mai, Laser shock processing and its effects on microstructure and properties of metal alloys: A review, *Int. J. Fatigue.* 24 (2002) 1021–1036.
- [1] A. Gill, A. Telang, S.R. Mannava, D. Qian, Y.S. Pyoun, H. Soyama, V.K. Vasudevan, Comparison of mechanisms of advanced mechanical surface treatments in nickel-based superalloy, *Mater. Sci. Eng. A.* 576 (2013) 346–355.
- [2] P. Peyre, R. Fabbro, P. Merrien, H.P. Lieurade, Laser shock processing of aluminium alloys. Application to high cycle fatigue behaviour, *Mater. Sci. Eng. A.* 210 (1996) 102–113.
- [3] U. Sánchez-Santana, C. Rubio-González, G. Gomez-Rosas, J.L. Ocaña, C. Molpeceres, J. Porro, M. Morales, Wear and friction of 6061-T6 aluminum alloy treated by laser shock processing, *Wear.* 260 (2006) 847–854.
- [4] S.A. Kumar, R. Sundar, S.G.S. Raman, H. Kumar, R. Gnanamoorthy, R. Kaul, K. Ranganathan, S.M. Oak, L.M. Kukreja, Fretting wear behavior of laser peened Ti-6Al-4V, *Tribol. Trans.* 55 (2012) 615–623.
- [5] A.S. Gill, Z. Zhou, U. Lienert, J. Almer, D.F. Lahrman, S.R. Mannava, D. Qian, V.K. Vasudevan, High spatial resolution, high energy synchrotron x-ray diffraction characterization of residual strains and stresses in laser shock peened Inconel 718SPF alloy, *J. Appl. Phys.* 111 (2012) 084904.

- [6] S. Amini, M. Dadkhah, R. Teimouri, Study on laser shock peening of Incoloy 800 super alloy, *Optik*. 140 (2017) 308–316.
- [7] W.F. He, Y.H. Li, Q.P. Li, H.L. Liu, Y.Q. Li, R.J. Liu, The effects of laser shock peening on fatigue life in Ni-based superalloy, *Adv. Mater. Res.* 135 (2010) 209–214.
- [8] Y. Fang, Y. Li, W. He, Y. Lu, P. Li, Numerical simulation of residual stresses fields of DD6 blade during laser shock processing, *Mater. Des.* 43 (2013) 170–176.
- [9] Y. Li, L. Zhou, W. He, G. He, X. Wang, X. Nie, B. Wang, S. Luo, Y. Li, The strengthening mechanism of a nickel-based alloy after laser shock processing at high temperatures, *Sci. Technol. Adv. Mater.* 14 (2013) 055010.
- [10] A.S. Gill, A. Telang, V.K. Vasudevan, Characteristics of surface layers formed on inconel 718 by laser shock peening with and without a protective coating, *J. Mater. Process. Technol.* 225 (2015) 463–472.
- [11] J.Z. Lu, K.Y. Luo, Y.K. Zhang, G.F. Sun, Y.Y. Gu, J.Z. Zhou, X.D. Ren, X.C. Zhang, L.F. Zhang, K.M. Chen, C.Y. Cui, Y.F. Jiang, A.X. Feng, L. Zhang, Grain refinement mechanism of multiple laser shock processing impacts on ANSI 304 stainless steel, *Acta Mater.* 58 (2010) 5354–5362.
- [12] J.Z. Lu, K.Y. Luo, Y.K. Zhang, C.Y. Cui, G.F. Sun, J.Z. Zhou, L. Zhang, J. You, K.M. Chen, J.W. Zhong, Grain refinement of LY2 aluminum alloy induced by ultra-high plastic strain during multiple laser shock processing impacts, *Acta Mater.* 58 (2010) 3984–3994.
- [13] L. Chen, X. Ren, W. Zhou, Z. Tong, S. Adu-Gyamfi, Y. Ye, Y. Ren, Evolution of microstructure and grain refinement mechanism of pure nickel induced by laser shock peening, *Mater. Sci. Eng. A.* 728 (2018) 20–29.
- [14] L. Chen, Y. Sun, L. Li, X. Ren, Microstructural evolution and mechanical properties of selective laser melted a nickel-based superalloy after post treatment, *Mater. Sci. Eng. A.* 792 (2020) 139649.
- [15] M. Rozmus-Górnikowska, J. Kusiński, Ł. Cieniek, J. Morgiel, The

- microstructure and properties of laser shock peened CMSX4 superalloy, *Metall. Mater. Trans. A.* 52 (2021) 2845–2858.
- [16] X. Chen, C. Dejoie, T. Jiang, C.S. Ku, N. Tamura, Quantitative microstructural imaging by scanning Laue x-ray micro- and nanodiffraction, *MRS Bull.* 41 (2016) 445–453.
- [17] B.C. Larson, L.E. Levine, Submicrometre-resolution polychromatic three-dimensional X-ray microscopy, *J. Appl. Crystallogr.* 46 (2013) 153–164.
- [18] R.C. Reed, C.M.F. Rae, Physical metallurgy of the nickel-based superalloys, in: D.E. Laughlin, K. Hono (Eds.), *Physical Metallurgy*, Elsevier, Oxford, 2014, pp. 2215–2290.
- [19] ASTM International, Standard test method for Vickers hardness of metallic materials, 1992.
- [20] M. Kunz, N. Tamura, K. Chen, A.A. MacDowell, R.S. Celestre, M.M. Church, S. Fakra, E.E. Domning, J.M. Glossinger, J.L. Kirschman, G.Y. Morrison, D.W. Plate, B.V. Smith, T. Warwick, V.V. Yashchuk, H.A. Padmore, E. Ustundag, A dedicated superbend x-ray microdiffraction beamline for materials, geo-, and environmental sciences at the advanced light source, *Rev. Sci. Instrum.* 80 (2009) 035108.
- [21] N. Tamura, XMAS: a versatile tool for analyzing synchrotron x-ray microdiffraction data, in: R.I. Barabash, G. Ice (Eds.), *Strain and Dislocation Gradients from Diffraction: Spatially-Resolved Local Structure and Defects*, Imperial College Press, London, 2014, pp. 125–155.
- [22] J. Kou, K. Chen, N. Tamura, A peak position comparison method for high-speed quantitative Laue microdiffraction data processing, *Scr. Mater.* 143 (2018) 49–53.
- [23] T.W. Cornelius, D. Carbone, V.L.R. Jacques, T.U. Schüllli, T.H. Metzger, Three-dimensional diffraction mapping by tuning the X-ray energy, *J. Synchrotron Radiat.* 18 (2011) 413–417.
- [24] G. Zhou, J. Kou, Y. Li, W. Zhu, K. Chen, N. Tamura, Quantitative Scanning

- Laue Diffraction Microscopy: Application to the study of 3D printed nickel-based superalloys, *Quantum Beam Sci.* 2 (2018) 13.
- [25] G. Zhou, W. Pantleon, R. Xu, W. Liu, K. Chen, Y. Zhang, Quantification of local dislocation density using 3D synchrotron monochromatic X-ray microdiffraction, *Mater. Res. Lett.* 9 (2021) 183–189.
- [26] M. Wilkens, The determination of density and distribution of dislocations in deformed single crystals from broadened X-ray diffraction profiles, *Phys. Status Solidi.* 2 (1970) 359–370.
- [27] G. Liu, J.S. Cantó, S. Winwood, K. Rhodes, S. Biroasca, The effects of microstructure and microtexture generated during solidification on deformation micromechanism in IN713C nickel-based superalloy, *Acta Mater.* 148 (2018) 391–406.
- [28] D. Karthik, S. Swaroop, Laser shock peening enhanced corrosion properties in a nickel based Inconel 600 superalloy, *J. Alloys Compd.* 694 (2017) 1309–1319.
- [29] G.X. Lu, J.D. Liu, H.C. Qiao, Y.Z. Zhou, T. Jin, J.B. Zhao, X.F. Sun, Z.Q. Hu, Effect of laser shock on tensile deformation behavior of a single crystal nickel-base superalloy, *Mater. Sci. Eng. A.* 686 (2017) 46–53.
- [30] I. Altenberger, E.A. Stach, G. Liu, R.K. Nalla, R.O. Ritchie, An in situ transmission electron microscope study of the thermal stability of near-surface microstructures induced by deep rolling and laser-shock peening, *Scr. Mater.* 48 (2003) 1593–1598.
- [31] M.S. Schneider, B. Kad, D.H. Kalantar, B.A. Remington, E. Kenik, H. Jarmakani, M.A. Meyers, Laser shock compression of copper and copper-aluminum alloys, *Int. J. Impact Eng.* 32 (2006) 473–507.
- [32] G.E. Ice, R.I. Barabash, White beam microdiffraction and dislocations gradients, *Dislocations in Solids.* 13 (2007) 499–601.
- [33] W. Shockley, W.T. Read, Quantitative predictions from dislocation models of crystal grain boundaries, *Phys. Rev.* 75 (1949) 692.
- [34] S.J. Lainé, K.M. Knowles, P.J. Doorbar, R.D. Cutts, D. Rugg, Microstructural

- characterisation of metallic shot peened and laser shock peened Ti–6Al–4V, *Acta Mater.* 123 (2017) 350–361.
- [35] A.S. Gill, A. Telang, C. Ye, S.R. Mannava, D. Qian, V.K. Vasudevan, Localized plastic deformation and hardening in laser shock peened Inconel alloy 718SPF, *Mater. Charact.* 142 (2018) 15–26.
- [36] L.E. Murr, J.-Y. Huang, Effect of shock-stress duration on the residual structure and hardness of nickel, chromel and inconel, *Mater. Sci. Eng.* 19 (1975) 115–122.
- [37] N. Hansen, Hall-Petch relation and boundary strengthening, *Scr. Mater.* 51 (2004) 801–806.
- [38] G.I. Taylor, The mechanism of plastic deformation of crystals. Part I.—Theoretical, *Proceedings of the Royal Society of London. Series A, Containing Papers of a Mathematical and Physical Character.* 145 (1934) 362–387.
- [39] F.X. Kayser, C. Stassis, The elastic constants of Ni<sub>3</sub>Al at 0 and 23.5 °C, *Phys. Status Solidi.* 64 (1981) 335–342.
- [40] D. Tabor, *The hardness of metals*, Clarendon Press, Oxford, 1951.